Advanced Composites and Hybrid Materials (2025) 8:155
https://doi.org/10.1007/s42114-024-01173-1

RESEARCH

Boron nitride nanotubes induced strengthening in aluminum 7075 composite via cryomilling and spark plasma sintering

Sohail M. A. K. Mohammed[1] · **Ambreen Nisar**[1] · **Denny John**[1] · **Abhijith K. Sukumaran**[1] · **Yifei Fu**[2] · **Tanaji Paul**[1] · **Alexander F. Hernandez**[3] · **Sudipta Seal**[2] · **Arvind Agarwal**[1]

Received: 8 June 2024 / Revised: 17 October 2024 / Accepted: 13 December 2024

Abstract

Al7075 is among the strongest commercial aluminum alloys with low density, making it a standout choice for structural metals. However, the never-ending quest for higher strength and low-density materials demands structural metals stronger than Al7075. In this study, high-strength and chemically inert one-dimensional boron nitride nanotubes (BNNTs) are used to reinforce Al7075 alloy, making ultra-high strength aluminum matrix composite. Al7075-BNNT composite is fabricated using a multi-step process involving ultrasonication, cryomilling, and spark plasma sintering (SPS). Ultra-fine grains were efficiently achieved in 2 h of milling, resulting in an impressive ultimate strength of ~ 636.8 ± 18.9 MPa and elongation up to necking of 10.1 ± 0.5% in heat-treated Al7075-BNNT composite. The obtained strength is 1.3 times higher than SPS Al7075 and 2.9 times higher than cast Al7075 alloy. The cryomilling facilitated a homogeneous dispersion of BNNTs, fostering effective interfacial bonding, albeit leading to variations in BNNT length ranging from 1–50 μm. The interplay between BNNT lengths and their impact on mechanical properties is explored, showcasing a synergistic improvement in strength and elongation. The comprehensive understanding of the resulting strengthening mechanisms encompasses Hall–Petch, Orowan, dislocation-induced strengthening, and dominant load transfer mechanisms. These findings offer valuable insights into fabricating high-performance aluminum matrix composites surpassing conventional strength. The Al7075-BNNT composite's unprecedented mechanical strength could further extend the use of aluminum alloys to more demanding aerospace applications, such as spacecraft structures and next-generation vehicles, as well as racing and automotive parts where the need for ultra-lightweight yet ultra-strong materials is paramount for fuel efficiency and performance under extreme conditions.

Keywords Al7075 · BNNT · Deformation · Spark plasma sintering · Strengthening mechanisms

1 Introduction

Al7075 alloy (Al–Zn–Mg–Cu) is a precipitation-strengthened alloy that is widely used in automobile, aerospace, marine industries, and other transportation applications that demand high strength, elevated temperature properties, and corrosion resistance [1]. Although Al7075 is considered as lightweight and strongest aluminum alloy, its strength proves insufficient for applications requiring exceptionally high strength by maintaining their low density. Several attempts have been made to further improve the strength of Al7075 by micro and nano reinforcements like nanotubes, carbides, nitrides, oxides, etc., that are much stronger and stiffer than the matrix [2–4]. The addition of these high-strength particles into a soft aluminum matrix results in a metal matrix composite (MMC) that demonstrates mechanical properties positioned between those of the matrix and the

✉ Arvind Agarwal
agarwala@fiu.edu

[1] Cold Spray and Rapid Advanced Deposition Laboratory (ColRAD), Department of Mechanical & Materials Engineering, Florida International University, 10555 West Flagler Street, Miami, FL 33174, USA

[2] Advanced Materials Processing and Analysis Center, Department of Materials Science & Engineering, University of Central Florida, Orlando, FL 32816, USA

[3] Advanced Materials Engineering Research Institute (AMERI), Department of Mechanical & Materials Engineering, Florida International University, 10555 West Flagler Street, Miami, FL 33174, USA

reinforcement. The reinforcement of nano-sized particles, particularly nanotubes, is reported to be more beneficial and influential in exhibiting high strengthening effects and offering further superior mechanical properties and multifunctionality for structural applications [5, 6]. However, reinforcement like carbon nanotubes (CNTs) and graphene hinder the processing window as the reinforcements start oxidizing beyond 400 °C [7]. The existing research on the architectural design of CNT and graphene-reinforced composite demonstrated some promise in industrial sectors, yet the evolution of defects in CNTs at higher processing temperatures is still a concern [8, 9]. Boron nitride nanotubes (BNNTs), a structural analog of CNTs, are extraordinary material with remarkable mechanical strength (>30 GPa), high Young's modulus (~ 1 TPa), excellent thermal conductivity (up to 2000 W/m–K), high aspect ratio ($\sim$30 000–70 000) and excellent radiation shielding properties, besides high thermal and oxidation resistance [6, 7, 10, 11]. The interwall bonding forces and shear resistance between boron (B) and nitrogen (N) are much stronger due to covalent bonding than in Carbon, C – C bond in CNTs, which exhibits higher fracture strength [12]. Owing to higher oxidation resistance and chemical inertness up to a temperature of 900 °C, BNNTs offer wider processing windows as reinforcement material in MMCs [13]. As such, high-strength MMCs with multi-functional properties can be fabricated by retaining the structural and chemical integrity of BNNTs at elevated temperatures.

To date, several studies have proved that BNNTs can significantly improve the mechanical properties of aluminum matrix composites [14–20]. However, most of the work is reported on pure aluminum matrix, and the maximum strength of the BNNT-reinforced aluminum composite reported is roughly 400 MPa, which is lower than the conventional Al7075 alloy. The knowledge of the synergistic effect of alloying elements and BNNTs is thus unexplored. Therefore, it is deemed imperative to study the mechanical properties and the underlying strengthening mechanisms of the Al7075-BNNT composite. The dispersion of BNNTs in the matrix is critical for utilizing the full potential of their strengthening effects. The high van der Waals forces within the reinforcement tend to limit their uniform dispersion in the metal matrix [21–23]. The most commonly used dispersion techniques include ball milling, ultrasonication and nanoscale dispersion [24]. Ball milling, although effective, requires extended periods and generates significant heat from friction and particle shearing. Huang et al. [21] reported high shear strain produced by high-pressure torsion (HPT) fragmented the agglomerated graphene nanoplates (GNPs) in the aluminum matrix and distributed the particles homogeneously through the advent of turbulent flow. However, the authors reported some agglomerates even after a high number of HPT turns which remains the challenge of reinforcement dispersion in metal matrix. At high shear strains and high temperatures of dispersion, the material undergoes dynamic recrystallization which increases the strength of the material but at the cost of severe ductility loss. Xie et al. [23] reported consolidation of composites at lower temperatures avoids nucleation of detrimental interfacial compounds. Thus, cryomilling, milling at cryogenic temperatures using liquid nitrogen, offers a sustainable alternative, enabling quicker, more homogeneous dispersion and reduced heat generation [25]. This method enhances interfacial bonding between BNNTs and aluminum, leading to better particle distribution and mechanical properties of the composite. Additionally, Spark Plasma Sintering (SPS) is employed for rapid, controlled densification of the cryomilled powder. SPS applies high electric fields and pressure to achieve a dense, fine-grained structure while maintaining the nanoscale features of BNNTs. This process prevents the formation of undesirable interfacial compounds, preserving the composite's ductility [26, 27]. Therefore, combining cryomilling and SPS ensures the fabrication of MMCs with uniformly dispersed nanotubes, optimizing mechanical properties [28, 29]. In addition, the high heating and cooling rates involved in SPS prevent excessive grain growth, favoring the densification of MMCs [30]. Earlier studies have demonstrated excellent microstructural and mechanical properties of CNT-reinforced aluminum composites via powder metallurgy routes, which lay a solid foundation for the present work [31, 32].

This study delves into the fabrication, microstructural features, and improvement of the mechanical strength of Al7075 by BNNT reinforcement, exploring the synergistic effects of cryomilling and SPS in the composite manufacturing process. The combined influence of cryomilling and SPS techniques not only refines the microstructure but also imparts unprecedented mechanical properties of the composite in sintered and heat-treated conditions. Additionally, the strengthening mechanisms, including grain refinement, load transfer and dislocation strengthening, are explored. Thus, this work contributes to the evolving landscape of advanced materials, providing valuable insights into the fabrication of high-strength BNNT-reinforced MMCs for superior performance and high-temperature applications.

2 Material and methods

2.1 Material processing

2.1.1 Powder processing

The starting powder utilized in this study is gas-atomized Al 7075 (Al-5.18 wt.% Zn-2.11 wt.% Mg-1.82 wt.% Cu) powder obtained from Valimet, Inc. (Stockton, CA), featuring an average particle diameter of approximately ~ 22 ± 17 µm. The powder corresponds to the Boeing Specification BMS 1067E, Type 10. Purified puffball BNNTs, produced by the pressurized vapor condensation method, were provided by BNNT, LLC (Newport News, Virginia). The reported average diameter and length of BNNTs are approximately ~ 5–10 nm and 100–200 µm, respectively, in as-received conditions [33]. These BNNTs are extensively entangled and agglomerated in bundled form. To disentangle BNNTs, a probe ultrasonic generator, Vibra-cell (VCX750, Sonics & Materials), operating at a frequency of 20 kHz with a maximum output power of 750 W, was employed. About 53 mg of BNNTs (1vol.% in the matrix) were probe sonicated in 40 mL isopropyl alcohol (IPA) at an amplitude of 30% for 30 min in an ice bath. Subsequently, Al7075 powder was added to the BNNT-IPA solution and subjected to probe sonication for 15 additional minutes, followed by drying in an ultrasonic bath at 80 °C for 4 h.

2.1.2 Nanostructured powders via cryo-milling

The feedstock powder was cryo-milled in liquid nitrogen (LN_2) for 12 h in a stainless-steel jar on CryoMill (Retsch, Germany). Liquid nitrogen was constantly supplied to the closed cryomill system in order to maintain the temperature at roughly −196 °C. Twenty grams of powder and 200 g of stainless-steel balls were used (powder-to-ball ratio: 1:10) for mixing in a dry environment. The milling was performed continuously at a frequency of 25 Hz for 2, 4 and 6 h. To ensure a consistent supply of liquid nitrogen, a pre-cooling step was performed for 5 min prior to milling. Subsequently, the milled powders were warmed to room temperature and collected in a sealed container in a controlled environment.

2.1.3 Spark plasma sintering

The cryo-milled powders were processed via spark plasma sintering (SPS, Model 104; Thermal Technologies, Santa Rosa, CA). The cryo-milled Al7075-BNNT powders were placed in a graphite die of 20 mm diameter, lined with a 1 mm thin graphite foil, to avoid adhesion between the sample and the die. The schematic of material fabrication is demonstrated in Fig. 1. The powders were sintered under vacuum at 500 °C with a heating rate of 100 °C/min. Uniaxial pressure was simultaneously increased to 60 MPa along with temperature and held for 10 min. The temperature was monitored using a thermocouple placed at the center of the die. Eventually, a cylindrical bulk sample of Al7075-1 vol.% BNNT with a diameter of 20 mm and thickness of 15 mm is obtained, as seen in Fig. 1. The Al7075 bulk sample was fabricated similarly without BNNTs for comparison. The densities of sintered Al7075 and Al7075-BNNT samples were measured using a pycnometer (Ultrapyc 5000, Anton Paar, Austria).

2.1.4 Heat treatment of sintered samples

The stability of the samples at elevated temperatures is investigated by performing heat treatment on the sintered samples. The heat treatment of powder is conducted inside a vacuum tube furnace (Lindberg/Blue M, USA) in two steps. Firstly, solution treatment at 475 °C for 4 h was performed, followed by rapid quenching in water to ambient temperature

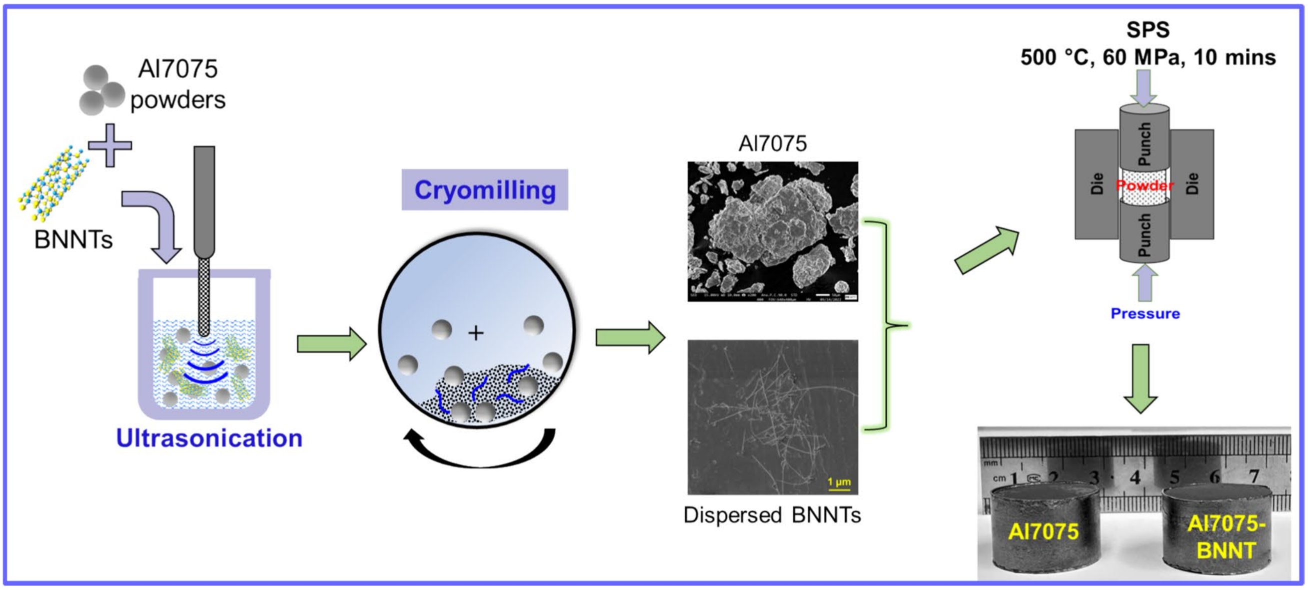

Fig. 1 Multi-step fabrication scheme of Al7075-BNNT composite by ultrasonication, cryomilling and SPS

to arrest the solute atoms from reprecipitation. Then, artificial aging was performed at 130 °C for 24 h in an inert environment, followed by natural cooling.

2.2 Characterization

2.2.1 Microstructure

The samples for the metallographic analysis were sectioned from the sintered and heat-treated sample using a high-speed diamond saw. The specimens were mechanically polished using #400 to #4000 grit SiC papers, followed by cloth polishing using alumina (1 µm) and colloidal silica (0.05 µm). No etching was performed on the samples. Energy dispersive X-ray spectroscopy (EDS) was performed to evaluate the elemental composition of the material. Samples for electron backscattered diffraction (EBSD) analysis were further polished on VibroMet (Versamet 3, Buehler) for 6 h. EBSD scans were conducted on a field-emission scanning electron microscope (SEM, JEOL F100) equipped with an EBSD detector (Symmetry S2, Oxford Instruments). The scans were performed at a step size of 15 nm and an accelerating voltage of 20 kV. The data were processed and analyzed using Aztec Crystal (Oxford Instruments). The Philips Tecnai F30 transmission electron microscope (TEM) was employed for cross-sectional imaging of the thin film Al-BNNT sample. The sample was extracted and thinned using an FEI 200 focused ion beam (FIB) system and mounted on PELCO FIB Lift-out Cu TEM grids. The identification of phases was accomplished via X-ray diffraction (XRD) using monochromatic Cu-Kα radiation on a Rigaku Smartlab Studio2 instrument. The measurements were conducted at an accelerating voltage of 40 kV, covering a diffraction angle range from 10° to 90°, and employing a scan rate of 0.2°/min.

2.2.2 Multiscale mechanical response

Localized mechanical properties of the fabricated specimens were measured using a nanoindenter (HIT 300, Anton Paar). The indents were performed on the polished samples employing Berkovich tip under load control with a peak load of 200 mN and a dwell time of 10 s. At least 5 indents were performed on each sample, and load–displacement data was evaluated using the Oliver and Pharr principle [34]. The hardness of the specimen is determined by dividing the peak load by the contact area. Tensile properties were assessed using profilometry-based indentation plastometry (PIP), an innovative technique offering an alternative to conventional testing. PIP is particularly advantageous for determining tensile properties of small-volume samples with high throughput, extracting information from a single indentation [35, 36]. The PIP testing procedure involves the estimation of true stress–strain curves through indentation, employing the iterative finite element method (FEM). Plastometrex (v.1.0) was utilized for PIP to evaluate the tensile properties of both Al and Al7075-BNNT composites, unraveling the strength enhancement in Al due to BNNT addition. Spherical indentations were made using a hard silicon nitride (Si_3N_4) indenter with a 2 mm diameter. The residual indent profile was systematically tracked along two orthogonal directions at the central point of the indentation using a stylus profilometer (Taylor Hobson, Talysurf) featuring a resolution of 0.4 µm. The indentation widths were contingent upon the material's load–displacement response. A linear variable displacement transducer (LVDT) with a resolution of 0.3 µm was utilized to regulate both the depth of the indenter and the positioning of the profilometer with respect to the sample [37]. For each sample, at least 4 indents were performed to calculate the average mechanical properties of the material. Analysis of variance (ANOVA) is performed to compare the significant difference between BNNT-reinforced composite and its counterpart Al7075 alloy. Single factor one-way ANOVA results with a confidence interval of 95% ($\alpha = 0.05$) are reported in supplementary Table S1 and S2.

3 Results

3.1 Powder modification

Al7075 powder and BNNTs are mixed in multiple steps to prepare a precursor. The average particle size of the as-received Al7075 powders was 22 ± 17 µm. The SEM images of as-received Al7075 powders are presented in Fig. 2(a_1)-(a_3). The BNNTs, after dispersion in IPA are mixed with Al7075 powders and ultrasonicated for 15 min. The detailed ultrasonic treatment on BNNTs and aluminum powder can be found elsewhere [24]. The resulting images of Al7075-BNNT powders after ultrasonication are presented in Fig. 2(b_1)-(b_3). Homogeneous dispersion on BNNTs is marked with yellow arrows. The EDS analysis of BNNTs on the Al7075 powder is presented in Supplementary Figure S1. Since ball milling generates heat due to cyclic severe plastic deformation, cooling the powders is an effective approach to accelerate the fracture processes and rapidly attain steady-state conditions. Hence, cryomilling is employed in this study. Cryomilling advantages include minimizing powder agglomeration, preventing oxidation, reducing milling time compared to room temperature processes, preserving dislocations, and allowing for potential higher dislocation density accumulation. It is important to highlight that while mechanically milling a mixture of Al7075 and BNNT, the ductile matrix remains susceptible to deformation, flattening, and cold welding, much like in the case

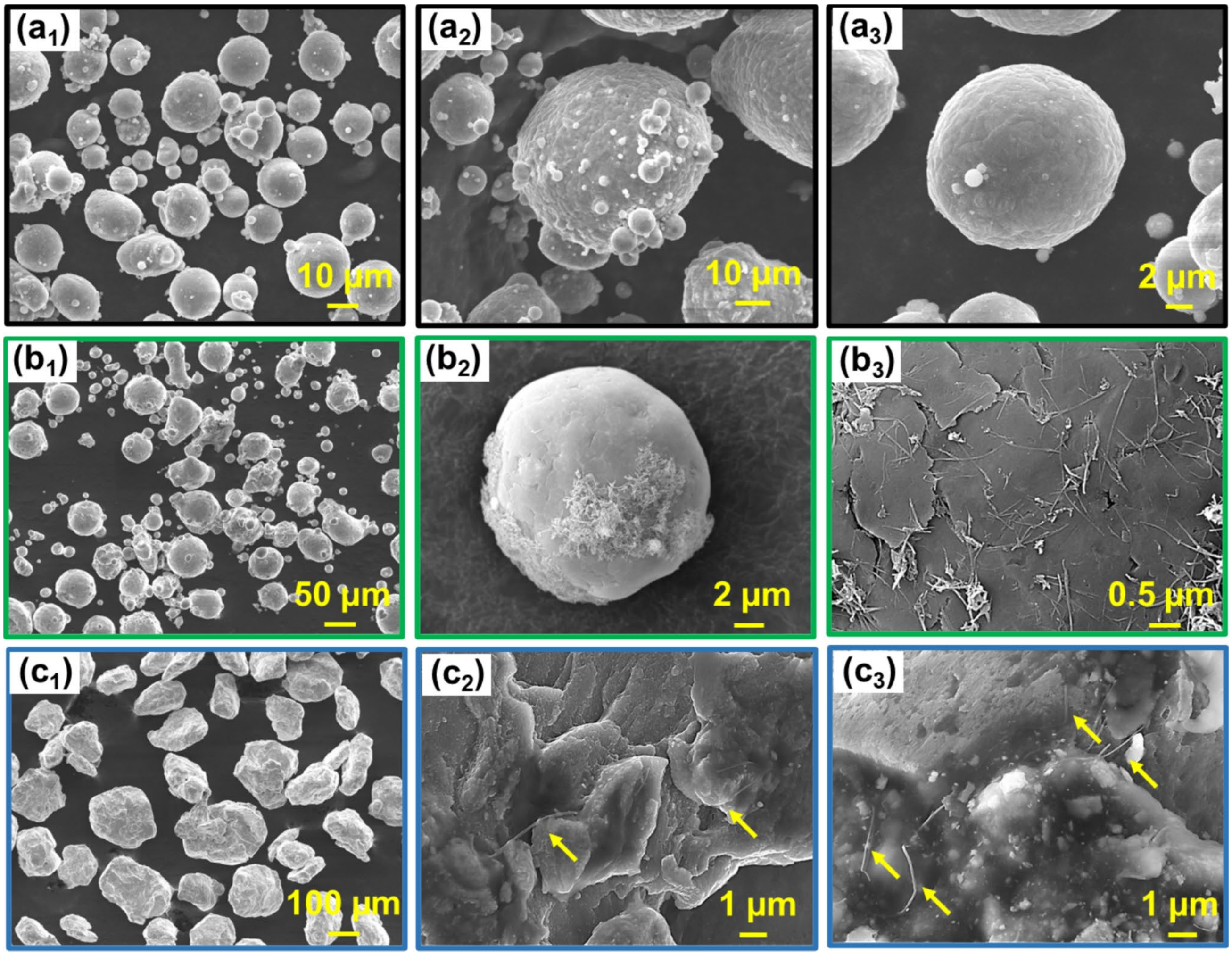

Fig. 2 SEM images of (**a**) As-received Al7075 powders, (**b**) Dispersion of BNNTs in Al7075 powders by UST, and (**c**) Bonding of BNNTs and Al7075 powder by cryomilling

of a monolithic metal. The presence of BNNTs does not hinder the grain refinement process in the matrix [38]. The initial morphology of powders from spherical with a diameter of ~ 22 ± 17 μm changed drastically irregular, flaky shape with severe interfacial defects and severe plastic deformation, as presented in Fig. 2(c_1)-(c_3). The size of the particles increased to ~ 152 ± 62 μm after 6 h of cryomilling. SEM images demonstrate the refinement of Al7075-BNNT powders as a function of milling time in supplementary Figure S2. Further, the broadening of XRD peaks and dislocation activity with respect to milling time is explained in supplementary Figure S3. The typical range of dislocation density in cold-rolled Al–Mg alloys is reported to be ~ 10^{15} m^{-2} [39]. The dislocation density of cryo-milled Al7075 powders is 4.2×10^{16} to 43×10^{16} m^{-2}, whereas for Al7075-BNNT powders, it increased up to 67×10^{16} m^{-2}. The variation of dislocation density and crystallite size with the milling time is presented in the supplementary Figure S4 (Section S3).

However, the refinement of grains during the milling process involves the formation of shear bands through localized deformation, followed by the propagation of these shear bands across the entire sample [40]. Insufficient milling time is often indicated by the presence of a few elongated grains in the milled powders. Thus, it is not surprising to observe microstructural features reflecting varying degrees of deformation rather than regular lognormal distributions of randomly oriented equiaxed grains. The initiation of fine grains is predominantly attributed to subdivisions and repeated fractures induced by milling at cryogenic temperatures, along with grain rotation and grain boundary sliding [41]. As milling time increased, the crystallite size in cryo-milled Al7075 and Al7075-BNNT gradually decreased, eventually reaching a saturated value of 26 nm and 21 nm, respectively, after 6 h of milling, as depicted in the supplementary

Figure S4. The cryomilling process, characterized by a cryogenic milling temperature, effectively suppresses recovery and recrystallization mechanisms, resulting in accelerated and rapid grain refinement.

3.2 Transition of cryo-milled powders to bulk sample

Efficient consolidation methods are essential for the widespread use of nanostructured powders, ensuring the production of desired bulk shapes in required sizes with near 100% theoretical density. Hence, SPS is employed in the present study. The microstructure of Al7075 and Al7075-BNNT samples after SPS and heat treatment are presented in Fig. 3a-d. The specimens were, in general, free from any visible porosity. However, due to the heat treatment, microporosity increased marginally. Consequently, a drop in density is recorded from 2.919 to 2.827 g/cm^3 in the Al7075 sample after heat treatment. Similarly, the density of the Al7075-BNNT sample decreased from 2.882 g/cm^3 in SPS condition to 2.780 g/cm^3 after heat treatment. The microstructure majorly consists of precipitates. Figure 3a and b depict homogeneously distributed irregularly shaped precipitates rich in Mg and Zn. However, few locations are

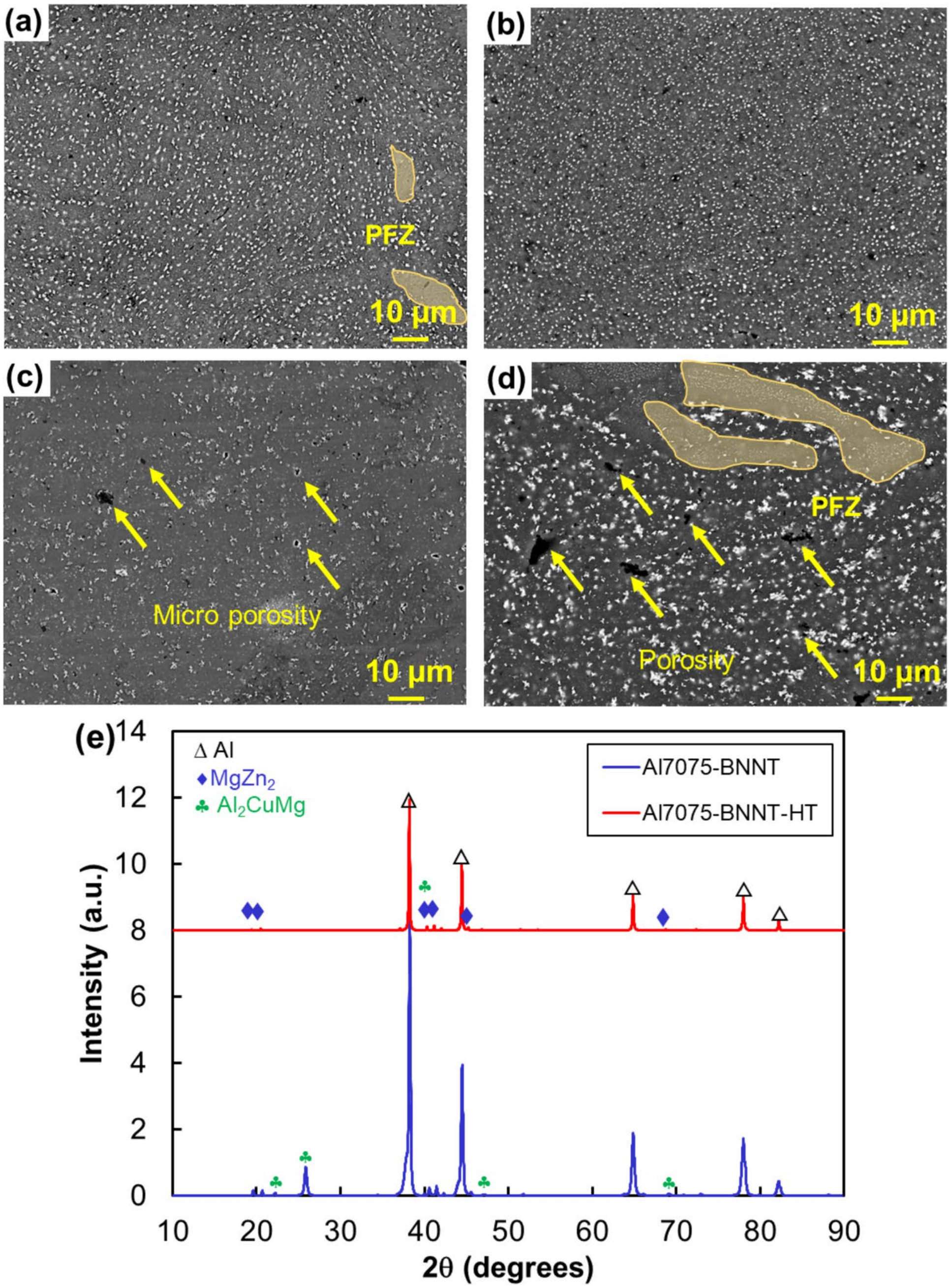

Fig. 3 SEM images showing the distribution of precipitates and increase in porosity with heat treatment of (**a**) Al7075, (**b**) Al7075-BNNT, (**c**) Al7075-HT and (**d**) Al7075-BNNT-HT, (**e**) XRD spectrum of Al7075-BNNT in the sintered and heat-treated condition

free from precipitates, often referred to as precipitate-free zones (PFZs). PFZs are formed due to insufficient diffusion of atoms during sintering but do not deteriorate the properties significantly. The addition of BNNTs resulted in slight coarsening of precipitates, especially post-heat treatment, as seen in Fig. 3d.

The XRD pattern of SPS processed bulk Al7075-BNNT composite in sintered and heat-treated conditions is presented in Fig. 3e. The pattern reveals the presence of a secondary phase (Al_2CuMg) and η-precipitate ($MgZn_2$) after SPS. It is well known that the primary elements of Al7075 alloy are Al, Cu, Mg and Zn. However, the room temperature solubility of Cu, Mg and Zn in Al is low, with the highest solubility exhibited by Mg (≤ 1.8 wt.%) [42]. In addition, the solubility of Cu in Al at eutectic temperature is ~ 2.5 at.%, but during SPS, due to the simultaneous application of temperature of 500 °C and high pressure of 60 MPa, solubility limit of Cu, Mg and Zn in Al increases and supersaturated solid solution can be formed. Hence, the presence of reported precipitates is expected. Following heat treatment, the secondary phase particles were dissolved in the matrix, and only $MgZn_2$ was present. The intensity of the XRD spectrum of bulk samples decreased compared to the powders, which indicates the evolution of grain growth or release of microstrain during the SPS process.

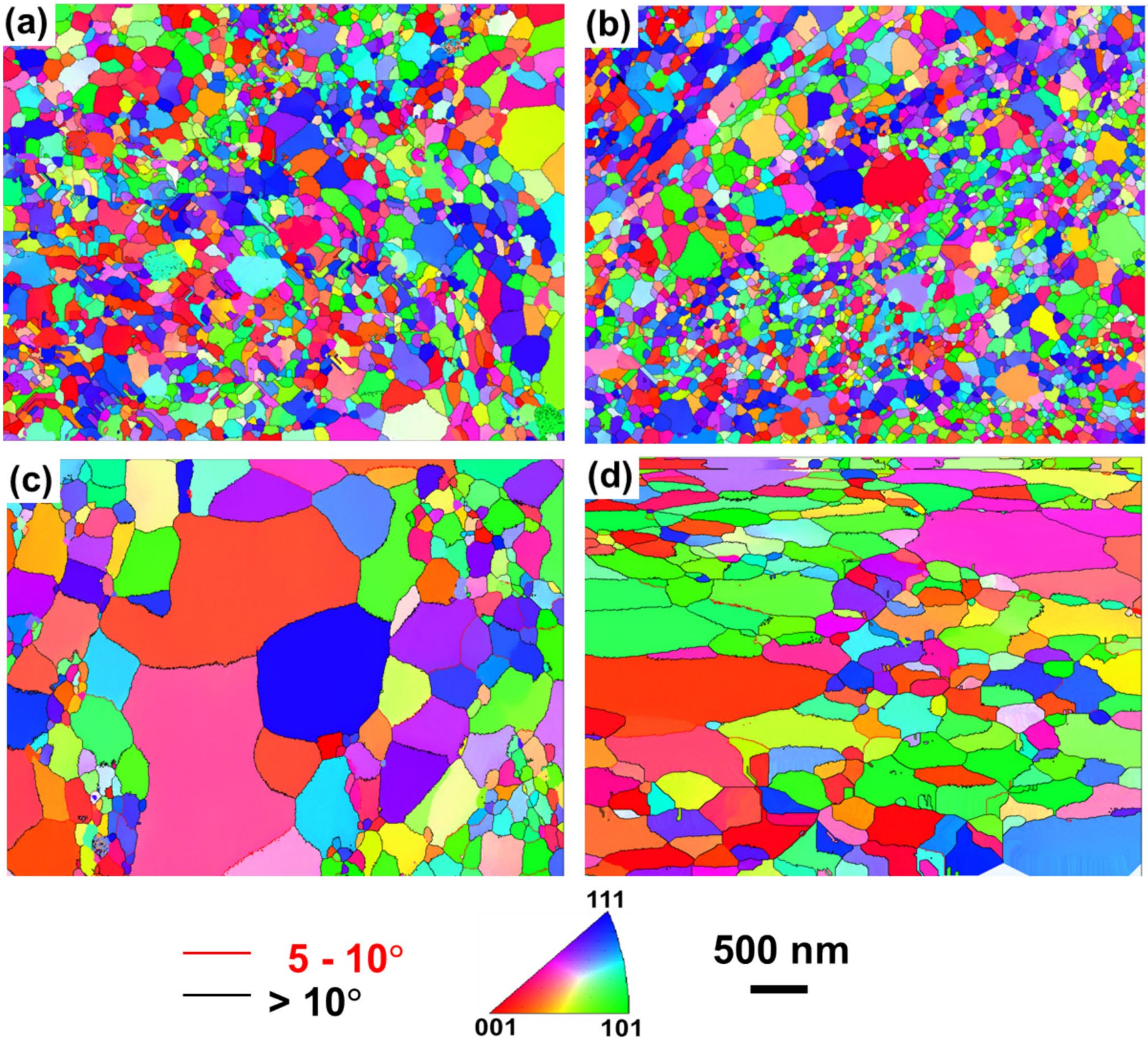

Fig. 4 EBSD orientation maps of (**a**) Al7075, (**b**) Al7075-BNNT, (**c**) Al7075-HT and (**d**) Al7075-BNNT-HT. The crystallographic orientation is represented with reference to the inverse pole figure of aluminum

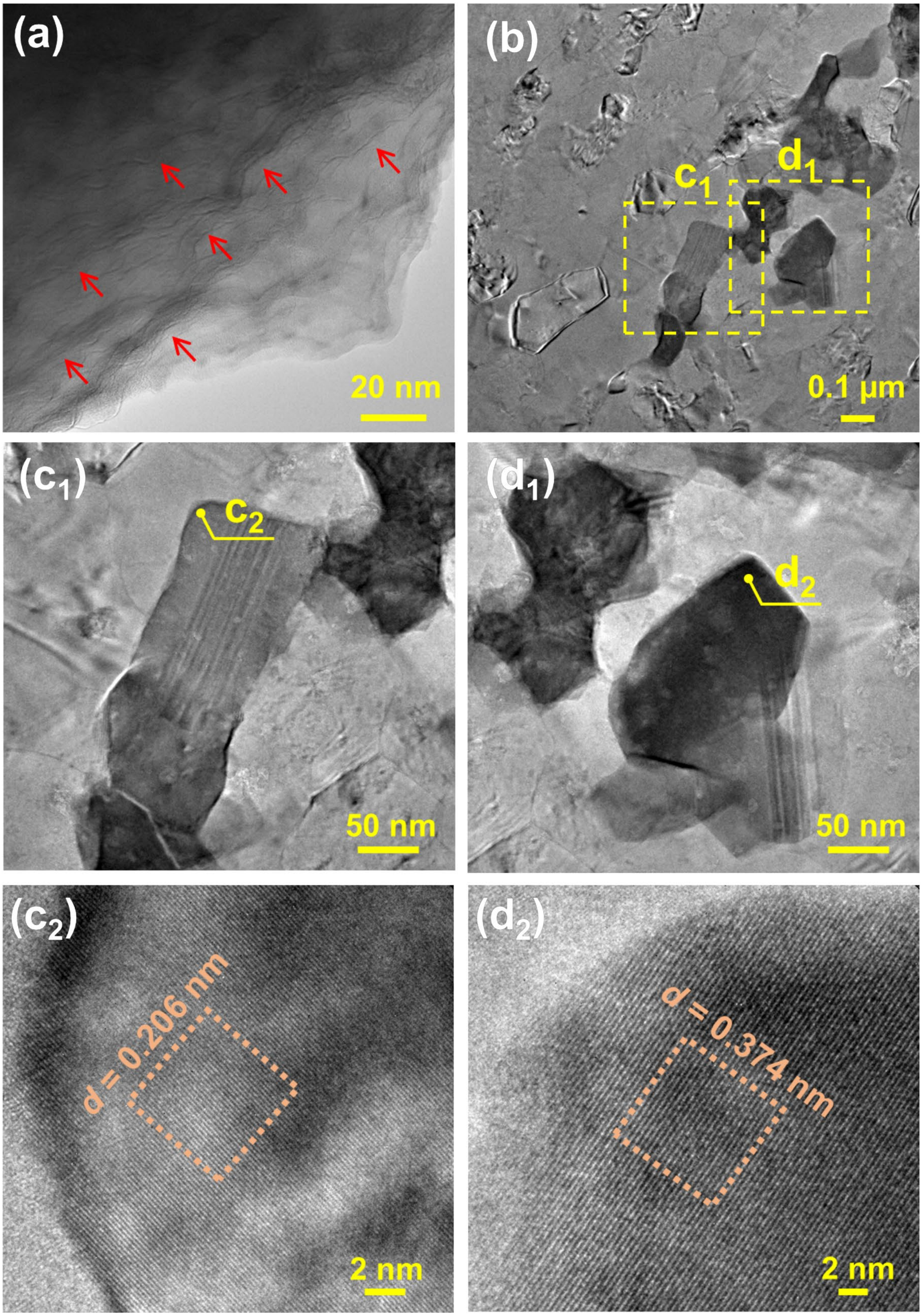
(a)
20 nm
(b)
c1
d1
0.1 µm
(c1)
c2
50 nm
(d1)
d2
50 nm
(c2)
d = 0.206 nm
2 nm
(d2)
d = 0.374 nm
2 nm

◀**Fig. 5** TEM images of Al7075-BNNT in heat treated condition showing (**a**) homogeneous dispersion of successfully retained BNNTs in the matrix, (**b**) aluminum matrix and formation of secondary precipitates, (c_1) lath like η-precipitate (d_1)hexagonal GP zone; (c_2) and (d_2) HRTEM images of interface between the precipitate and Al matrix

EBSD was carried out to study the grain morphology and crystal orientation of bulk samples. The orientation maps presented in Fig. 4a-d reveal that grains are nearly equiaxed and are randomly oriented without any specific crystallographic orientation. The composite is characterized by finer grains compared to Al7075 in sintered conditions. After heat treatment, the grain growth is evident, resulting from the dissolving of alloying elements and migration of solute atoms at a higher solution temperature of 475 °C. The average grain sizes evaluated from Aztec Crystal (assuming the grains to be circular) were found to be ~ 290 nm, ~ 240 nm, 650 nm, and 610 nm for Al7075, Al7075-BNNT, Al7075-HT and Al7075-BNNT-HT, respectively. However, a few coarse/large grains with a size of up to 2 μm in sintered and up to 6 μm in heat-treated conditions were also observed. Spark discharge is the primary factor for larger grains, which accelerates the grain growth during the sintering process [42]. The low angle (LAGB) and high angle grain boundaries (HAGB) are identified as 5 – 10° and > 10° and indicated by red and black lines, respectively, in the orientation maps. The fraction of LAGB increased with the reinforcement of BNNTs due to the pileup of dislocations at the interface of BNNTs and the matrix. LAGBs act as dislocation cells and allow the pileup of dislocations at the sites, eventually improving the material's mechanical strength. Similar observations were made by Sadeghi et al. [43], who reported an increase in strength with the fraction of LAGBs in CNT-reinforced Al matrix composites.

3.3 Evolution of secondary phases

TEM images in Fig. 5 represent the dispersion of BNNTs and precipitates in the matrix. The BNNTs are homogeneously dispersed, and no clusters of BNNTs are evident in the composite in heat-treated conditions, as demonstrated in Fig. 5a. The dispersed BNNTs are marked in red arrows, whereas precipitates are demarcated in yellow dotted lines. The homogeneous dispersion results from a mutual effect of ultrasonic treatment as well as efficient cryomilling followed by solid-state fusion. Moreover, the structural integrity of BNNTs is retained without any visible defects on the walls or inner surface. It must be noted that the composite was free from undesirable interfacial compounds like AlN and AlB_2, which are commonly reported in BNNT-reinforced aluminum matrix composites [26, 27]. This is because SPS was performed under vacuum at a relatively lower temperature of 500 °C and a lower duration of 10 min compared to the literature values.

The secondary phases of Al7075 alloy post-heat treatment have been reported extensively [44]. The microstructure consists of an aluminum matrix and a second phase η-$MgZn_2$ which are confirmed by XRD investigations (Figs. 3e and 5b). However, the effect of BNNTs on the precipitation phenomena is unexplored. TEM evaluated a detailed insight into the phase composition and precipitates for the Al-BNNT sample in cross-section f. For phase identification, a digital micrograph was used to measure the *d*-spacing of the precipitate at two different locations indicated in Fig. 5b. Precipitates are evident with a relatively large size of rough 1 μm with varying morphology, with no signs of Al_2CuMg precipitates. Two such precipitates – lath-shaped (Fig. 5(c_1)) and hexagonal-shaped (Fig. 5(d_1)) are further scrutinized using HRTEM analysis. The lath shaped precipitates are relatively large and are identified to be Mg and Zn rich η-precipitate. These large second-phase particles are located predominantly at grain boundaries or along triple points. The corresponding *d*-spacing of $MgZn_2$ was calculated from HRTEM images in Fig. 5(c_2) as 0.206 nm. The mismatch between the lattice planes of $MgZn_2$ and Al matrix suggests incoherency between these phases, resulting from the solution treatment of the Al-BNNT composite. Similarly, the hexagonal shape precipitates were identified to be rich in Mg and Zn as well. The *d*-spacing value of this phase was found to be 0.374 nm (Fig. 5(d_2)), which is in close agreement with the GP zones [45]. These findings further validate the presence of Mg-Zn precipitates and dissolution of Al-Cu precipitates confirmed by XRD results discussed earlier in Fig. 3e.

3.4 Mechanical properties and strain-hardening behavior

The tensile properties provide a comprehensive understanding of the material's response at a bulk scale, as per ASTM standards. However, the specimen dimensions in our study are confined to a diameter of 20 mm and thickness of ~ 15 mm, which falls short of meeting the requirements for conducting tensile tests following ASTM standards. Hence, we employed PIP in this study to assess mechanical properties. Despite being an indentation-based technique, PIP entails the deformation of a sufficiently large volume (> 1 mm diameter) to be representative of the bulk material, as it is widely accepted [46–48]. The estimation of tensile characteristics in PIP involves iterative FEM modeling, characterized by the Voce equation [47],

$$\sigma = \sigma_s - \left(\sigma_s - \sigma_y\right)\exp\left(\frac{-\varepsilon}{\varepsilon_0}\right) \tag{1}$$

where σ, σ_s, σ_y are the (von Mises) applied stress, saturation, and yield stress (YS), respectively; ε and ε_0 are the plastic (von Mises) and characteristic strain. Throughout the iterations, the FEM model optimizes Voce parameters to attain convergence. Subsequently, the plasticity parameters obtained through the best-fit process are utilized to estimate the mechanical properties of the specimens.

The PIP-derived tensile stress–strain curves of Al7075 and Al7075-BNNT in sintered and heat-treated conditions are presented in Fig. 6a and b. The average YS and ultimate tensile strength (UTS) of Al7075 alloy is ~ 377.8 ± 24.5 and 473 ± 20.5 MPa against 539.1 ± 9.9 and 542.5 ± 6.4 MPa for Al7075-BNNT composite. In comparison, the elongation up to necking (%El) of Al7075-BNNT decreased to 3.7 ± 1.9% compared to 14.1 ± 3.1% in Al7075 alloy. In this work, we have focused on elongation up to necking, a widely accepted measure of deformation before instability sets in [11, 24, 26]. While elongation to fracture was not captured, we believe elongation up to necking provides meaningful insights for a qualitative comparison of the effect of BNNT addition on plastic deformability. The obvious increase in the YS by ~ 25.2% and with considerable elongation in the Al7075-BNNT composite is due to the reinforcement of high-strength BNNTs and the precipitates presented in Fig. 5. The YS and UTS of Al7075 fabricated by SPS in the present study are in close agreement with the strength of conventional Al7075 alloy and much higher than the stir-cast Al7075 [49]. The presence of BNNTs offers more grain boundaries, which eventually leads to a superior strength based on the Hall–Petch relationship. This also suggests a robust interfacial bonding and load-transfer efficiency between the matrix and BNNTs. However, a trade-off in ductility is observed with the increase in strength. Nevertheless, a high strengthening efficiency (η_s) of ~ 1470% was achieved as calculated from,

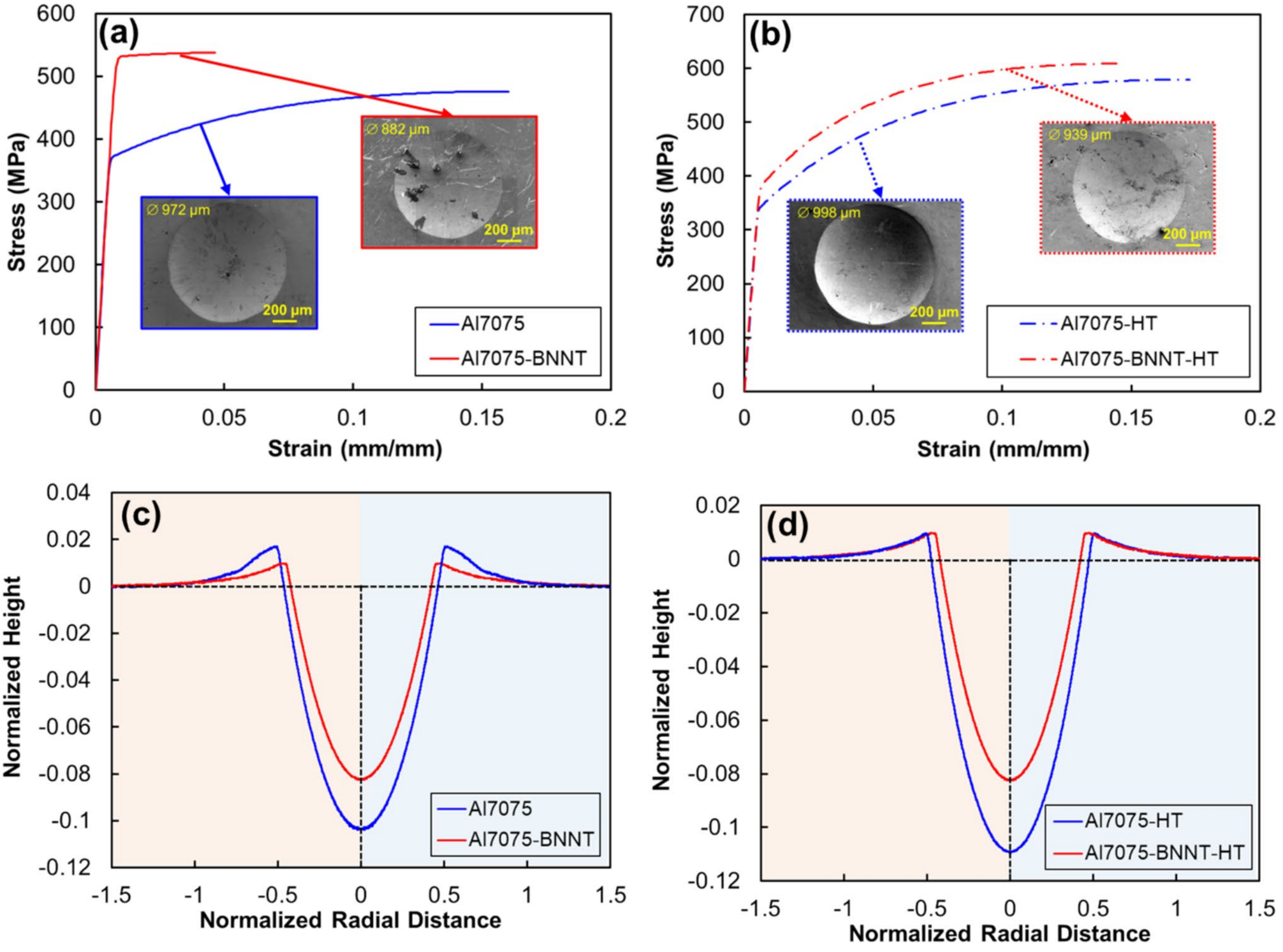

Fig. 6 PIP derived stress–strain curves of Al7075 and Al7075-BNNT composite in (**a**) Sintered and (**b**) heat-treated condition; profilometry of PIP indention in (**c**) Sintered and (**d**) heat-treated condition

Table 1 Mechanical and physical properties of Al7075 and Al7075-BNNT composite in sintered and heat-treated conditions

Material	YS	UTS	%EL	ρ (gm/cm^3)	HV$_{0.05}$
Al7075	377.8 ± 24.5	473 ± 20.5	14.05 ± 3.1	2.919 ± 0.04	164.8 ± 24.0
Al7075-BNNT	539.1 ± 9.9	542.5 ± 6.4	3.65 ± 1.9	2.882 ± 0.05	215.8 ± 8.8
Al7075-HT	299.5 ± 52.3	541.3 ± 37.5	16.7 ± 1.9	2.827 ± 0.01	150.3 ± 13.0
Al7075-BNNT-HT	395.0 ± 45.1	636.8 ± 18.9	10.1 ± 0.5	2.780 ± 0.02	204.8 ± 23.7

$$\eta_s = \frac{\sigma_c - \sigma_m}{V_{BNNT}\sigma_m}, \tag{2}$$

where σ_c and σ_m is the UTS of the composite and matrix, respectively, and V_{BNNT} is the volume fraction of BNNTs. Such a remarkable strengthening efficiency is due to the mutual effect of homogeneous dispersion of BNNTs load transfer ability of high aspect ratio BNNTs used in this study. The PIP indents of both Al7075 and Al7075-BNNT are presented as inset in the stress–strain plot to corroborate the indentation pile-up with mechanical properties. The indents are very symmetrical, indicating the bulk sample has isotropic mechanical properties. In addition, the diameter of the PIP indent on Al7075 is ~ 971.8 µm compared to 881.6 µm in the Al7075-BNNT composite, revealing the high resistance to plastic deformation in the composite offered by the presence of high-strength BNNTs. Similarly, the diameter of PIP indents in heat-treated conditions is 998 and 938.7 µm for Al7075 and Al7075-BNNT composite, respectively. The larger diameter of the indents in heat-treated conditions reflects the lower yield strength of the material. The pile-up of indentations of sintered and heat-treated samples are compared in Fig. 6c and d, where a higher pile-up is observed in Al7075 compared to Al7075-BNNT. The normalized height of the pile-up zone is 0.0172 and 0.0098 in Al7075 and Al7075-BNNT, respectively. Similarly, in heat-treated conditions, it is 0.0099 and 0.0096 in Al7075 and Al7075-BNNT, respectively. The height of the pile-up zone has an inverse relationship with the YS of the material [50], which confirms the lower YS value of Al7075 compared to its composite in both sintered and heat-treated conditions (Table 1).

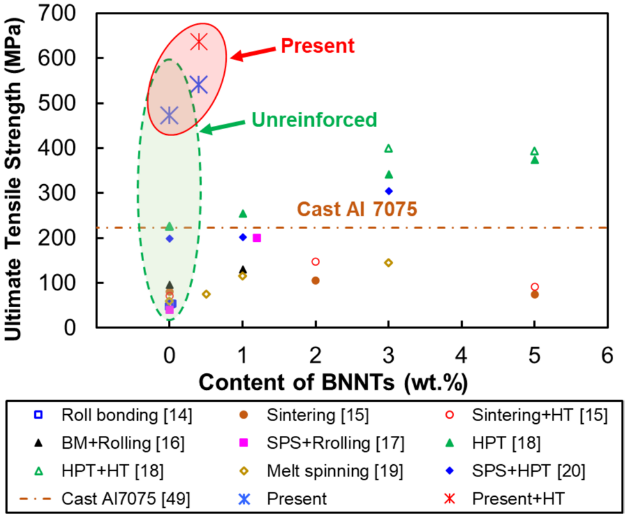

Fig. 7 Ultimate tensile strength of BNNT-reinforced Al composites with varying BNNT contents compared with the present materials [14–20, 49]

Table 2 Strain hardening coefficients of Al7075 and Al7075-BNNT

Material	n	K
Al7075	0.1357	702.6
Al7075-BNNT	0.0303	615.9
Al7075-HT	0.2275	1031.1
Al7075-BNNT-HT	0.2137	1077.3

Since the material with poor ductility cannot find significant usage for structural applications, heat treatment is performed to improve the ductility. After heat treatment (solution treatment + artificial aging), a decrease in YS but a dramatic increase in UTS and elongation up to necking in both Al7075 and Al7075-BNNT composite is achieved, as presented in Fig. 7. The decrease in YS stems from the dissolution of secondary phase Al_2CuMg due to prolonged solution treatment of 4 h. Nevertheless, the material exhibited strain hardening capacity and resulted in improved UTS from 473 ± 20.5 to 541.3 ± 37.5 MPa in Al7075, whereas 542.5 ± 6.4 to 636.8 ± 18.9 MPa in Al7075-BNNT attributed to heat treatment. The increase is about 14.4% and 17.0% in Al7075 and Al7075-BNNT composite compared to sintered conditions. The improvement in elongation is observed in both materials but is more pronounced in the Al7075-BNNT composite. The strain hardening coefficient/strengthening coefficient and exponent are studied in detail and evaluated using the Hollomon equation [51]:

$$\sigma = K\varepsilon^n \tag{3}$$

σ, ε, K, and n are true stress, true strain, strength coefficient, and strain hardening exponent, respectively. The evaluated n and K values of Al7075 and Al7075-BNNT in sintered and heat-treated conditions are presented in Table 2. The strain hardening parameters of both Al7075 and Al7075-BNNT increased with heat treatment.

A summary of the tensile properties of BNNT-reinforced Al7075 alloys in comparison with the present alloy and existing Al7075-BNNT composites is summarized in Fig. 7 [14–20, 49]. It is seen that the present material possesses significantly higher strength and significant elongation. The UTS of the current composite is compared with similar BNNT-reinforced aluminum composites produced using various fabrication techniques, along with their respective base alloys as a function of volume fraction. The UTS of the present materials is positioned above that of conventional Al7075 alloy. Such superior strengths of the present Al7075 and Al7075-BNNT are extraordinary compared to even high-strength aluminum alloys. By increasing the volume fraction of BNNTs and controlling the heat treatment process, the strength of Al7075 can be further increased and achieve ultra-high strength nanocomposites to answer the never-ending quest for higher strength and low-density materials.

3.5 Localized hardness and elastic modulus response

The localized elastic modulus and nanohardness of the materials are investigated by the nanoindentation technique. The typical load–displacement curve of the Al7075-BNNT composite is compared with its pure Al7075 base material in Fig. 8a, showing the distinct loading, holding, and unloading regions. The curves are smooth and free from any abnormalities or pop-in effects. For an identical peak load of 200 mN, the indentation depth of Al7075 is ~ 2054 nm as opposed to ~ 1751 nm in the Al7075-BNNT composite. This shows that the addition of hard BNNTs offers increased resistance to plastic deformation. The observed behavior can be attributed to the increased resistance to dislocation activities due to the hard and impenetrable BNNTs in the matrix. The strengthening effect of BNNTs in the composite is evident as the load–displacement curve shifted towards the left and exhibited lower displacement. Hence, the Young's modulus of Al-BNNT is higher compared to Al7075. It is obvious that the reinforcement of BNNTs results in enhanced modulus as well as hardness of the composite. The reduced modulus of the sample based on Young's modulus of indenter and sample is obtained as,

$$\frac{1}{E_r} = \left(\frac{1 - {v_s}^2}{E}\right) + \left(\frac{1 - {v_i}^2}{E_i}\right) \tag{4}$$

where ν is the Poisson ratio, and E is the Young's modulus. The subscripts "s" and "i" represent sample and Berkovich indenter, respectively. The Young's modulus of the indenter is 1140 GPa, and the Poisson's ratio is 0.07. The summary of estimated average hardness as well as average modulus values are presented in Fig. 8b. The average hardness value increased from 1.6 ± 0.2 GPa in Al7075 to 2.2 ± 0.4 GPa with the reinforcement of BNNTs. Similarly, improvement in modulus is observed from 70.9 ± 0.4 GPa in Al7075 to 79.1 ± 5.4 GPa in the Al7075-BNNT composite. Using the rule of mixtures (ROM), for 1 vol.% of BNNTs, the elastic modulus is estimated to be 78.5 GPa, which is in close agreement with the experimental value; such improvement in hardness and modulus stems from the load transfer mechanism from the matrix to BNNTs which will be discussed in the later section. The higher stiffness in Al7075-BNNT composite with a low standard deviation is driven by homogeneous dispersion of BNNTs resulting from ultrasonication and cryomilling of powders.

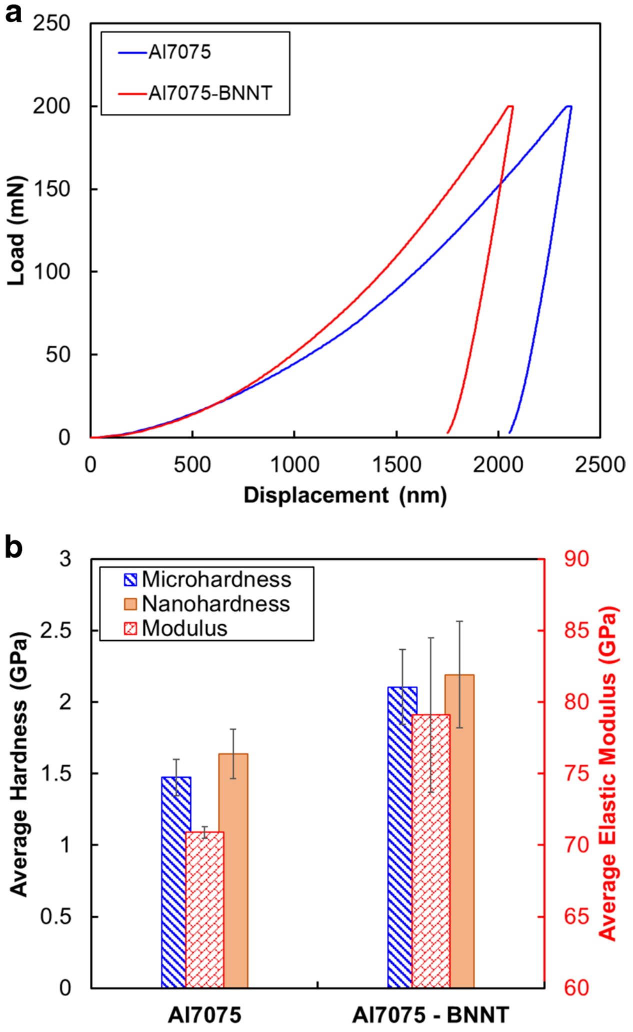

Fig. 8 **a** Characteristic load–displacement curves, and (**b**) Hardness and Modulus of Al7075 and Al7075-BNNT composite

The enhancement observed in the nanohardness and elastic modulus values of the Al7075-BNNT composite, in contrast to the unreinforced Al7075, can be attributed to the fact that during nanoindentation, the active source of dislocation at the pointed end of the indenter induces a significant surge in atomic activities, leading to the accumulation of strain. This phenomenon, combined with the presence of BNNTs within the composites, impedes dislocation movement, causing the buildup of dislocations at grain boundaries. Additionally, the microhardness of the alloy and composite in sintered and heat-treated conditions is presented in Table 1. The average microhardness of Al7075 and Al7075-BNNT in the sintered condition is 164.8 ± 24.0 and 215.8 ± 8.8 HV, respectively. Similarly, the average microhardness in heat-treated conditions is found to be 150.3 ± 13.0 and 204.8 ± 23.7 HV, respectively. In general, the presence of coherent and finely dispersed $MgZn_2$ phases formed during sintering hinders the dislocation motion and thus improves the hardness [52]. However, the decrease in the hardness after heat treatment is attributed to the dissolution of secondary phases during solution treatment at 475 °C, as confirmed by XRD peaks in Fig. 3e and TEM observations in Fig. 5.

4 Discussion

Due to extensive dispersion from ultrasonication and cryomilling, the length of the BNNTs appeared to be smaller, ranging from ~ 1 to 50 µm compared to the as-received 100–200 µm. The average length of the BNNTs was still found to be larger than the critical length (L_c = ~ 394 to 789 nm) required for effective load transfer in the Al7075 matrix. Thus, the use of high aspect ratio BNNTs in the present study provides crack-bridging and effective strengthening in the composite. Since a variation in the length of BNNTs exists, the interplay of strengthening mechanisms is potentially possible. The predominant strengthening mechanisms contributed by BNNTs in composites include Hall–Petch strengthening ($\Delta\sigma_{HP}$), Orowan strengthening ($\Delta\sigma_{OR}$), dislocation strengthening ($\Delta\sigma_{DD}$) and load-transfer effect ($\Delta\sigma_{LT}$) [53, 54]. Then, the YS of the composite could be predicted as [54],

$$\sigma_{yc} = \sigma_{ym}\left(1 + f_{HP}\right)\left(1 + f_{OR}\right)\left(1 + f_{DD}\right)\left(1 + f_{LT}\right), \tag{5}$$

where σ_{ym} is the YS of alloy matrix, f_{HP}, f_{LT}, f_{OR}, and f_{DD} are the enhancement factors related to Hall–Petch, Orowan, dislocation and load-transfer strengthening, respectively, defined as the consequent strength improvement divided by σ_{ym} [54]. In other words, Eq. (5) can be re-written as,

$$\sigma_{yc} = \sigma_{ym}\left(1 + \frac{\Delta\sigma_{HP}}{\sigma_{ym}}\right)\left(1 + \frac{\Delta\sigma_{OR}}{\sigma_{ym}}\right)\left(1 + \frac{\Delta\sigma_{DD}}{\sigma_{ym}}\right)\left(1 + \frac{\Delta\sigma_{LT}}{\sigma_{ym}}\right), \tag{6}$$

The compounding method of estimation is used in the present study, which demonstrated a high level of accuracy in nanotube-reinforced MMCs compared to the arithmetic or quadratic method [55]. The grain refinement strengthening is often predicted by the Hall–Petch mechanism, which is given by:

$$f_{HP} = \frac{k\left(d_c^{-1/2} - d_m^{-1/2}\right)}{\sigma_{ym}}, \tag{7}$$

where k is the Hall–Petch constant (= 0.13 MPa-m$^{1/2}$ for Al alloy [56]), which is considered to be a quantity of the grain boundary's resistance to slip transfer. Utilizing the average grain sizes obtained from EBSD analysis, i.e., $d_m = 290$ nm for Al7075 and $d_c = 240$ nm for Al7075-BNNT, the Hall–Petch strengthening is estimated at ~ 23.9 MPa.

Additionally, the movement of dislocations can be hindered by hard and impenetrable BNNTs due to the strong B-N bonds and the high strength of BNNTs, leading to the formation of dislocation loops. As dislocations within the Al matrix glide over the slip plane, they generate Orowan loops because of interaction with and bypassing the BNNTs. A higher stress level is required to facilitate more dislocations bypassing BNNTs, resulting in an increased presence of Orowan loops around BNNTs and, consequently, an enhancement in material strength. The improvement factor attributed to Orowan looping strengthening is quantified by the Orowan-Ashby equation [57],

$$f_{OR} = \frac{0.84MG_m b}{\sigma_{ym}\pi d_{eq}\sqrt{(1-\nu)}\left(\sqrt{\frac{3\pi}{2V_{BNNT}}} - \frac{\pi}{4}\right)} ln\left(\frac{\pi d_{eq}}{8b}\right), \tag{8}$$

where M is the Taylor factor (3.06 for FCC [58]), G_m is the shear modulus ($G_m = E_m/[2 \times (1 + \nu)]$), b is Burgers vector of aluminum (0.286 nm), ν is the Poisson's ratio of aluminum alloy (0.33). The equivalent diameter d_{eq} of BNNTs is determined by a spherical model as [59],

$$d_{eq} = \sqrt[3]{\frac{3}{2}L_{BNNT}d_{BNNT}^2}, \tag{9}$$

where L_{BNNT} is the average length, and d_{BNNT} is the average diameter of BNNTs (~ 7.5 nm). The Orowan increment $\Delta\sigma_{\mathrm{OR}}$ is evaluated to be ~ 21.2 MPa, suggesting that it is not the dominant strengthening mechanism due to the high aspect ratio of the BNNTs in the present study. Although shortening of BNNTs by cryomilling is observed, the length of the BNNTs was much higher than the critical length. The lower contribution by Orowan can be further explained by dislocation sink on the interaction of dislocation with BNNTs, something that is common in long and high aspect ratio BNNTs, as shown in schematic Fig. 9. It is difficult for the dislocations to bypass or shear the hard and long BNNTs when the length is higher than the critical length, as discussed earlier. Eventually, the dislocations sink at the walls of the BNNTs in the present study. In contrast, if the shearing of BNNTs is severe, which is common during ball

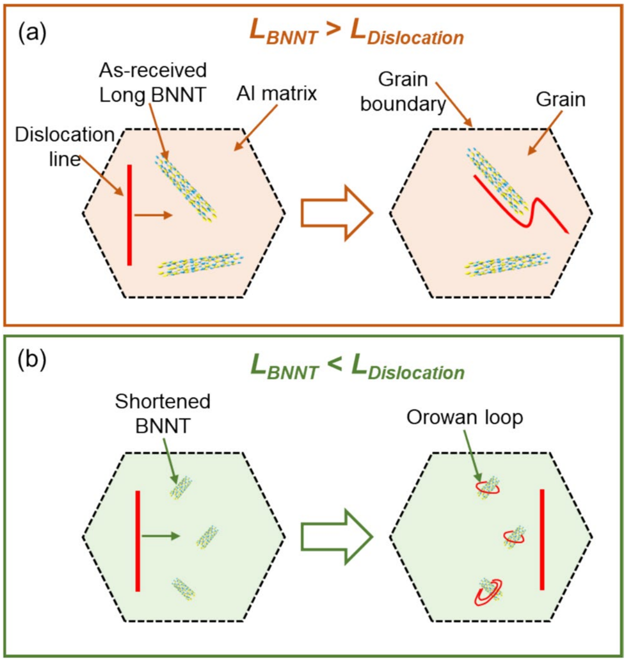

Fig. 9 Dislocation movement on interaction with (**a**) long and high aspect ratio BNNTs and (**b**) short BNNTs resulting from severe shearing

milling compared to cryomilling, the length of the BNNTs is reduced greatly. In such a case, the dislocations bow around BNNTs, leaving an Orowan loop in their wake over the slip plane (see Fig. 9b). In addition to microscale investigation, the validation of the length-dependent strengthening-mode transition can be related to elongation. Besides strength, elongation can be dependent on the interaction of dislocations and BNNTs. In long BNNTs, as represented in Fig. 9a, the pinned dislocations result in increased plastic strains and potential crack initiation sites at the interface following the Kelly-Tyson model [60]. Thus, at macro/mesoscale, the elongation will be reduced with an increase in strength attributed to BNNT reinforcement, which is obvious in the mechanical properties presented in Fig. 6a and Table 1.

In the composite, the presence of BNNTs can induce prismatic punching of dislocations at the interface, contributing to an augmentation in the material's work hardening discussed earlier. This phenomenon is attributed to the variation in coefficients of thermal expansion between BNNTs and the aluminum matrix. Hence, the enhancement factor in dislocation strengthening, arising from the increased dislocation density, can be mathematically expressed as,

$$f_{DD} = \frac{kG_m b\sqrt{\Delta\rho}}{\sigma_{ym}}, \tag{10}$$

where k is a constant (~ 1.25 [54]) and $\Delta\rho$ is the increased dislocation density stemming from the BNNT and aluminum thermal mismatch-induced additional dislocations in the composite relative to Al7075. The dislocation density is evaluated from the XRD patterns, which could be estimated as [61],

$$\rho = \frac{\beta^2}{4.35b^2}, \tag{11}$$

where β ($=\beta_{obs} - \beta_{inst}$) represents the full width at half maximum (FWHM) of Al peaks with β_{obs} and β_{inst} denoting the observed and instrumental peak broadening, respectively. The computation of dislocation density is conducted on the most closely packed plane (111) identified through XRD analysis. The XRD analysis reveals a calculated increment in dislocation density for the current nanocomposite relative to its base alloy is evaluated to be $1.8 \times 10^{13}\ \mathrm{m}^{-2}$. Subsequently, the $\Delta\sigma_{DD}$ is estimated to be 40.4 MPa. This substantial increment can be attributed to the bending of high aspect ratio BNNTs (Fig. 9a), leading to increased back stress and strain hardening [62]. Sadeghi et al. [63] reported an increase in dislocation density by CNTs due to an effective increase in high back stress via accumulation and hindering of dislocation annihilation at the interfaces, and grain boundaries. It is noteworthy that the increased dislocations, as evidenced by residual stresses in composites, fundamentally arise from the differences in coefficients of thermal expansion between the matrix and reinforcement. Then, load transfer would be a pivotal strengthening mechanism, particularly in composites featuring aligned BNNTs, especially with high aspect ratios. Given that the average length of BNNTs surpasses the critical length, load transfer is likely to be the dominant strengthening mechanism. The load transfer increment factor can thus be measured as [53],

$$f_{LT} = \Delta\sigma - f_{HP} - f_{OR} - f_{DD}, \tag{12}$$

where $\Delta\sigma$ is the difference in the YS of composite and alloy. With the combination of the above strengthening effects, the predicted load transfer strengthening is evaluated to be 76.4 MPa, which is the dominant strengthening mechanism in the present composite. However, the effective load transfer is subjected to a clean interface between BNNTs and the matrix. The interfacial features between BNNTs and the aluminum matrix are detailed in our earlier studies [27]. The crack bridging phenomena are well-captured during nanoindentation, as presented in Fig. 10. The image shows the retained BNNT after the nanoindentation in the Al7075-BNNT composite. The indentation was performed with a peak load of 200 mN, which is sufficient to deform the matrix; however, no deformation of BNNT was observed, which demonstrates the high strength of the BNNTs. The length of the BNNT is ~ 17 µm, which is greater than the critical length required for effective load transfer. In addition, the formation of a tribofilm-like layer is also observed at one

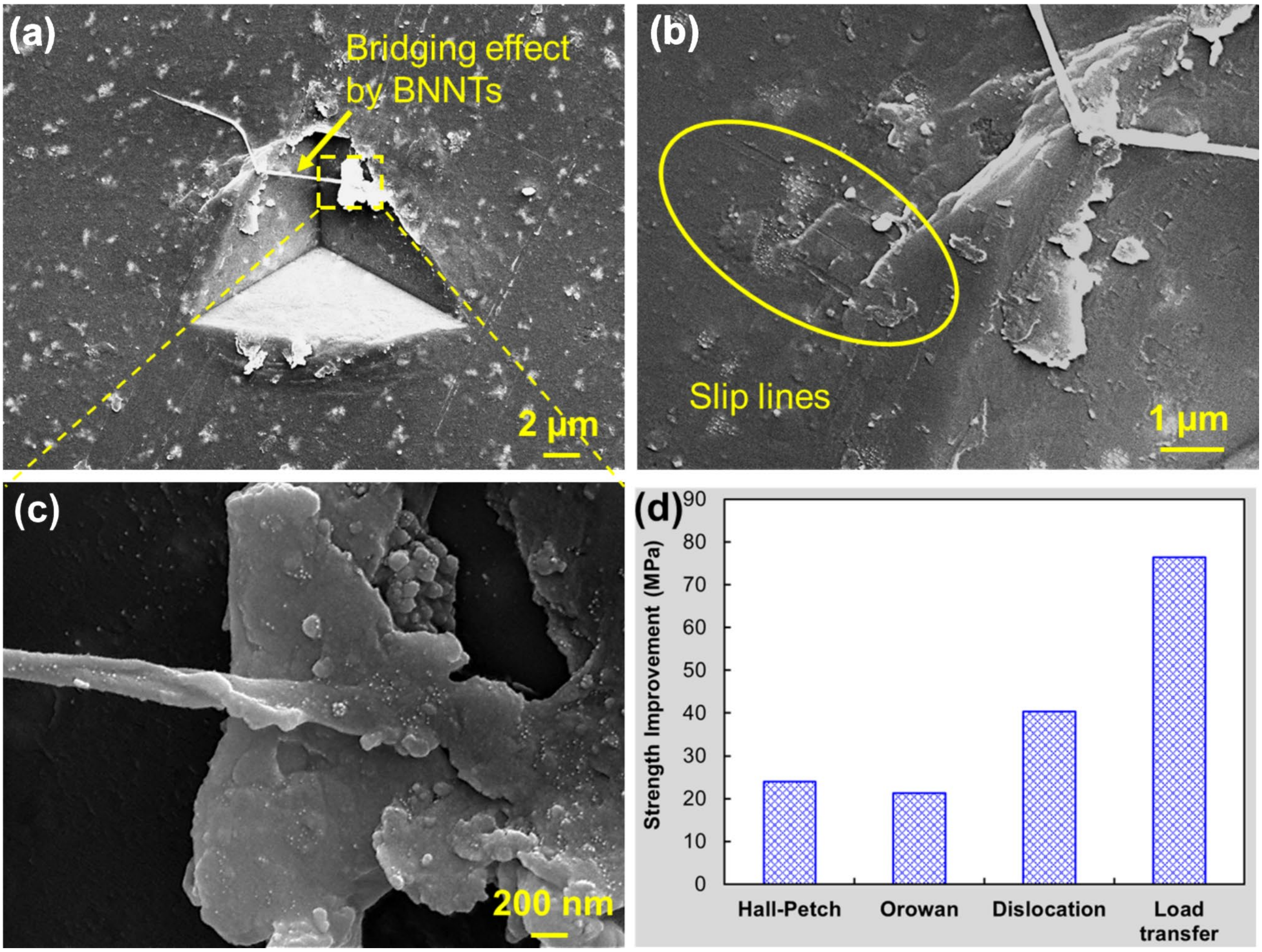

Fig. 10 **a** –(**c**) Stress-bridging mechanism by BNNTs during nanoindentation at a load of 200 mN; (**d**) Contribution of strengthening mechanism in the composite

end of the nanotube in Fig. 10c. Since BNNTs have excellent lubricating properties, they offer wear resistance and reduce friction between the indenter and the aluminum matrix due to compressive load, resulting in the shearing of B-N layers, leading to the formation of a thin film. The formation of a tribofilm-like layer further demonstrates a strong adhesion between the BNNTs and matrix. Thus, BNNT can enhance the application of composites with multi-functional properties. This further confirms that BNNTs played a significant role in load transfer strengthening in the present composite compared to other strengthening mechanisms. The summary of strength improvement by the major strengthening mechanisms is presented in Fig. 10d, with load transfer as the dominant strengthening mechanism with a contribution of 76.4 MPa.

Finally, the overall high strength of the present nanocomposite is a result of the coupled effects of these composite-specific strengthening mechanisms along with the presence of varying lengths of BNNTs resulting from ultrasonic treatment and cryomilling. The controlled consolidation by vacuum sintering and heat treatment enhanced the mechanical properties. Thus, BNNT-reinforced composites are promising candidates for achieving superior mechanical performance with balanced high strength and elongation along with multi-functional properties.

However, the current limitation of scalability of manufacturing and size of the specimen in this study needs to be addressed for their extended use in high-strength applications. The use of sequential steps, such as ultrasonication and cryomilling, requires precise control over process parameters (e.g., milling time, temperature, and ultrasonic energy). This makes it difficult to maintain consistent quality when transitioning to larger production volumes. While SPS is effective for achieving high-density and fine microstructures in small samples, scaling it up to process larger components for large aerospace or automotive structures is not straightforward. Limitations in SPS chamber size and non-uniform heating across larger samples could lead to residual stresses, defects, or microstructural inconsistencies. To address these limitations, future research could focus on developing alternative fabrication routes that simplify the process, such as exploring different powder consolidation techniques or utilizing scalable hybrid processing methods that maintain the unprecedented mechanical properties of the present study while reducing energy and equipment costs.

5 Conclusions

The integration of boron nitride nanotubes (BNNTs) into Al7075 through ultrasonication, cryomilling and spark plasma sintering has demonstrated its remarkable potential to result in a metal matrix composite that surpasses the mechanical strength of the high-strength aluminum alloy Al7075. The cryomilling for a shorter duration of 6 h effectively dispersed BNNTs and improved adhesion between BNNTs and aluminum, while spark plasma sintering demonstrated excellent consolidation of the composite. Microstructural analysis revealed the evolution of precipitates, GP zones and the unique interplay between BNNTs and the aluminum matrix. The multiscale mechanical properties derived by indentation-based techniques, including elastic modulus, YS, UTS and elongation up to necking, were significantly enhanced with the reinforcement of BNNTs. A remarkable UTS of ~ 636.8 ± 18.9 MPa is achieved in Al7075-BNNT composite in heat treated condition, which is 1.3 times higher compared to its unreinforced Al7075 and ~ 2.9 times higher compared to reported stir-cast Al7075 alloy. The dense bulk BNNT composite fabricated with a short 10 min holding time prevented the formation of undesirable interfacial compounds and thus retained elongation. The varying lengths of BNNTs contributed to synergistic improvement in strength and elongation. The strengthening mechanisms, such as grain refinement, dislocation strengthening and load-transfer mechanisms were investigated, and the load-transfer mechanism was found to be dominant. This study provides valuable insights into optimizing fabrication processes for high-performance composites, guiding future research in metal matrix composites to achieve superior mechanical properties. Additionally, enhancement in the strength of Al7075 extends its applications to next-generation vehicles and their parts.

Supplementary Information The online version contains supplementary material available at https://doi.org/10.1007/s42114-024-01173-1.

Acknowledgements The authors thank Dr. Roy Whitney of BNNT, LLC. for providing nanotube samples used in this work. Advanced Materials Engineering Research Institute (AMERI) at FIU is acknowledged for the research facilities used in this study.

Author contributions Conceptualization: SM, TP, AA
Methodology: SM, AN, DJ, AS.
Formal analysis and investigation: SM, AN, YF.
Writing—original draft preparation: SM.
Writing—review and editing: AA.
Funding acquisition: AA.
Resources: TP, AH, SS, AA.
Overall Supervision: AA.

Funding The authors acknowledge the financial support from the Army Research Office (ARO) through Grant W911NF1910097 by the Program Officers Drs. Mike Bakas and Andrew Brown. The authors also acknowledge the support of DEVCOM - Army Research Laboratory (ARL) through grant W911NF2020256.

Data Availability Some of the data is also included as supporting information.

Other Data sets generated during the current study are available from the corresponding author on reasonable request.

Declarations

Competing interests The authors declare no competing interests.

References

1. Gharbi O, Kumar Kairy S, De Lima PR, Jiang D, Nicklaus J, Birbilis N (2019) Microstructure and corrosion evolution of additively manufactured aluminium alloy AA7075 as a function of ageing. Npj Mater Degrad 3:40. https://doi.org/10.1038/s41529-019-0101-6
2. Zhou X, Feng Z, Zhu L, Xu J, Miyagi L, Dong H, Sheng H, Wang Y, Li Q, Ma Y, Zhang H, Yan J, Tamura N, Kunz M, Lutker K, Huang T, Hughes DA, Huang X, Chen B (2020) High-pressure strengthening in ultrafine-grained metals. Nature 579:67–72. https://doi.org/10.1038/s41586-020-2036-z
3. Lin T-C, Cao C, Sokoluk M, Jiang L, Wang X, Schoenung JM, Lavernia EJ, Li X (2019) Aluminum with dispersed nanoparticles by laser additive manufacturing. Nat Commun 10:4124. https://doi.org/10.1038/s41467-019-12047-2
4. Agarwal A, Bakshi SR, Lahiri D (2017) Carbon Nanotubes: Reinforced Metal Matrix Composites, 1st Editio, CRC Press, Boca Raton. https://www.crcpress.com/Carbon-Nanotubes-Reinforced-Metal-Matrix-Composites/Agarwal-Bakshi-Lahiri/p/book/9781138113732
5. Xu R, Tan Z, Xiong D, Fan G, Guo Q, Zhang J, Su Y, Li Z, Zhang D (2017) Balanced strength and ductility in CNT/Al composites achieved by flake powder metallurgy via shift-speed ball milling.

Compos Part A Appl Sci Manuf 96:57–66. https://doi.org/10.1016/j.compositesa.2017.02.017

6. Mohammed S, Nautiyal P, Paul T, Zhang C, Agarwal A (2024) A critique on boron nitride nanotube reinforced metal matrix composites. Crit Rev Solid State Mater Sci 49:482–519. https://doi.org/10.1080/10408436.2023.2229867
7. Golberg D, Bando Y, Tang CC, Zhi CY (2007) Boron nitride nanotubes. Adv Mater 19:2413–2432. https://doi.org/10.1002/adma.200700179
8. Sadeghi B, Cavaliere P, Pruncu CI (2022) Architecture dependent strengthening mechanisms in graphene/Al heterogeneous lamellar composites. Mater Charact 188:111913. https://doi.org/10.1016/j.matchar.2022.111913
9. Sadeghi B, Cavaliere P, Pruncu CI, Balog M, Marques de Castro M, Chahal R (2024) Architectural design of advanced aluminum matrix composites: a review of recent developments. Crit Rev Solid State Mater Sci 49:1–71. https://doi.org/10.1080/10408436.2022.2078277
10. Wei X, Wang M-S, Bando Y, Golberg D (2010) Tensile tests on individual multi-walled boron nitride nanotubes. Adv Mater 22:4895–4899. https://doi.org/10.1002/adma.201001829
11. Bacca N, Zhang C, Paul T, Sukumaran AK, John D, Rengifo S, Park C, Chu S-H, Mazurkivich M, Scott W, Agarwal A (2022) Tribological and neutron radiation properties of boron nitride nanotubes reinforced titanium composites under lunar environment. J Mater Res 37:4582–4593. https://doi.org/10.1557/s43578-022-00708-w
12. Falin A, Cai Q, Santos EJG, Scullion D, Qian D, Zhang R, Yang Z, Huang S, Watanabe K, Taniguchi T, Barnett MR, Chen Y, Ruoff RS, Li LH (2017) Mechanical properties of atomically thin boron nitride and the role of interlayer interactions. Nat Commun 8:15815. https://doi.org/10.1038/ncomms15815
13. Dolbec R (2016) Boron nitride nanotubes: properties, synthesis and applications, millipore sigma. https://www.sigmaaldrich.com/US/en/technical-documents/technical-article/materials-science-and-engineering/microelectronics-and-nanoelectronics/boron-nitride-nanotubes (accessed December 9, 2022)
14. Antillon M, Nautiyal P, Loganathan A, Boesl B, Agarwal A (2018) Strengthening in boron nitride nanotube reinforced aluminum composites prepared by roll bonding. Adv Eng Mater 20:1800122. https://doi.org/10.1002/adem.201800122
15. Bisht A, Kumar V, Li LH, Chen Y, Agarwal A, Lahiri D (2018) Effect of warm rolling and annealing on the mechanical properties of aluminum composite reinforced with boron nitride nanotubes. Mater Sci Eng A 710:366–373. https://doi.org/10.1016/j.msea.2017.10.101
16. Bastwros K, Wifi A, Esawi A (2022) Synthesis, mechanical properties, and microstructure of dual-matrix (DM) aluminum-boron nitride nanotube (Al-BNNT) composites. Emergent Mater 5:553–563. https://doi.org/10.1007/s42247-022-00363-1
17. Nautiyal P, Rudolf C, Loganathan A, Zhang C, Boesl B, Agarwal A (2016) Directionally aligned ultra-long boron nitride nanotube induced strengthening of aluminum-based sandwich composite. Adv Eng Mater 18:1747–1754. https://doi.org/10.1002/adem.201600212
18. Xue Y, Jiang B, Bourgeois L, Dai P, Mitome M, Zhang C, Yamaguchi M, Matveev A, Tang C, Bando Y, Tsuchiya K, Golberg D (2015) Aluminum matrix composites reinforced with multi-walled boron nitride nanotubes fabricated by a high-pressure torsion technique. Mater Des 88:451–460. https://doi.org/10.1016/j.matdes.2015.08.162
19. Yamaguchi M, Pakdel A, Zhi C, Bando Y, Tang D-M, Faerstein K, Shtansky D, Golberg D (2013) Utilization of multiwalled boron nitride nanotubes for the reinforcement of lightweight aluminum ribbons. Nanoscale Res Lett 8:3. https://doi.org/10.1186/1556-276X-8-3
20. Yamaguchi M, Meng F, Firestein K, Tsuchiya K, Golberg D (2014) Powder metallurgy routes toward aluminum boron nitride nanotube composites, their morphologies, structures and mechanical properties. Mater Sci Eng A 604:9–17. https://doi.org/10.1016/j.msea.2014.02.086
21. Huang Y, Bazarnik P, Wan D, Luo D, Pereira PHR, Lewandowska M, Yao J, Hayden BE, Langdon TG (2019) The fabrication of graphene-reinforced Al-based nanocomposites using high-pressure torsion. Acta Mater 164:499–511. https://doi.org/10.1016/j.actamat.2018.10.060
22. Xie Y, Meng X, Chang Y, Mao D, Qin Z, Wan L, Huang Y (2022) Heteroatom modification enhances corrosion durability in high-mechanical-performance graphene-reinforced aluminum matrix composites. Adv Sci 9(23):2104464. https://doi.org/10.1002/advs.202104464
23. Xie Y, Meng X, Chang Y, Mao D, Yang Y, Xu Y, Wan L, Huang Y (2022) Ameliorating strength-ductility efficiency of graphene nanoplatelet-reinforced aluminum composites via deformation-driven metallurgy. Compos Sci Technol 219:109225. https://doi.org/10.1016/j.compscitech.2021.109225
24. Mohammed SMAK, Paul T, John D, Zhang C, Agarwal A (2023) Understanding the role of ultrasonic cavitation assisted casting of boron nitride nanotube-reinforced aluminum matrix composite. J Mater Res Technol 25:2405–2418. https://doi.org/10.1016/j.jmrt.2023.06.111
25. Zhang X, Wang H, Narayan J, Koch CC (2001) Evidence for the formation mechanism of nanoscale microstructures in cryomilled Zn powder. Acta Mater 49:1319–1326. https://doi.org/10.1016/S1359-6454(01)00051-9
26. Mohammed SMAK, Aleman AA, John D, Paul T, Agarwal A (2023) Exploring the potential of wire fed direct energy deposition of aluminum-boron nitride nanotube composite: microstructural evolution and mechanical properties. Adv Eng Mater 25:1438–1656. https://doi.org/10.1002/adem.202300770
27. Nautiyal P, Gupta A, Seal S, Boesl B, Agarwal A (2017) Reactive wetting and filling of boron nitride nanotubes by molten aluminum during equilibrium solidification. Acta Mater 126:124–131. https://doi.org/10.1016/j.actamat.2016.12.034
28. Xu T, Wang Y, Liu K, Zhao Q, Liang Q, Zhang M, Si C (2023) Ultralight MXene/carbon nanotube composite aerogel for high-performance flexible supercapacitor. Adv Compos Hybrid Mater 6:108. https://doi.org/10.1007/s42114-023-00675-8
29. Thomson KE, Jiang D, Yao W, Ritchie RO, Mukherjee AK (2012) Characterization and mechanical testing of alumina-based nanocomposites reinforced with niobium and/or carbon nanotubes fabricated by spark plasma sintering. Acta Mater 60:622–632. https://doi.org/10.1016/j.actamat.2011.10.002
30. Cavaliere P, Sadeghi B, Shamanian M, Ashrafizadeh F (2019) Al-based nanocomposites produced via spark plasma sintering: effect of processing route and reinforcing phases. In: Spark Plasma Sinter. Mater., Springer International Publishing, Cham, pp. 161–190. https://doi.org/10.1007/978-3-030-05327-7_6
31. Sadeghi B, Cavaliere P (2022) CNTs reinforced Al-based composites produced via modified flake powder metallurgy. J Mater Sci 57:2550–2566. https://doi.org/10.1007/s10853-021-06665-9
32. Sadeghi B, Fan G, Tan Z, Li Z, Kondo A, Naito M (2022) Smart mechanical powder processing for producing carbon nanotube reinforced aluminum matrix composites. KONA Powder Part J 39:2022004. https://doi.org/10.14356/kona.2022004
33. BNNT LLC (2014) Boron nitride nanotubes–Technical Data, Virginia, USA, USA. https://www.bnnt.com/images/tech_data/documents/BNNT_P1_Beta_Tech_Data_1.2.pdf. Accessed 12 Dec 2024
34. Oliver WC, Pharr GM (1992) An improved technique for determining hardness and elastic modulus using load and displacement sensing indentation experiments. J Mater Res 7:1564–1583. https://doi.org/10.1557/JMR.1992.1564

35. Campbell JE, Kalfhaus T, Vassen R, Thompson RP, Dean J, Clyne TW (2018) Mechanical properties of sprayed overlayers on superalloy substrates, obtained via indentation testing. Acta Mater 154:237–245. https://doi.org/10.1016/j.actamat.2018.05.043
36. Venkatraman A, McDowell DL, Kalidindi SR (2022) Bayesian analysis of parametric uncertainties and model form probabilities for two different crystal plasticity models of lamellar grains in α+β Titanium alloys. Int J Plast 154:103289. https://doi.org/10.1016/J.IJPLAS.2022.103289
37. Campbell JE, Gaiser-Porter M, Gu W, Ooi S, Burley M, Dean J, Clyne TW (2022) Indentation plastometry of very hard metals. Adv Eng Mater 2101398:1–10. https://doi.org/10.1002/adem.202101398
38. Jiang L, Wen H, Yang H, Hu T, Topping T, Zhang D, Lavernia EJ, Schoenung JM (2015) Influence of length-scales on spatial distribution and interfacial characteristics of B4C in a nanostructured Al matrix. Acta Mater 89:327–343. https://doi.org/10.1016/j.actamat.2015.01.062
39. Zhou F, Liao X, Zhu Y, Dallek S, Lavernia E (2003) Microstructural evolution during recovery and recrystallization of a nanocrystalline Al-Mg alloy prepared by cryogenic ball milling. Acta Mater 51:2777–2791. https://doi.org/10.1016/S1359-6454(03)00083-1
40. Fan GJ, Choo H, Liaw PK, Lavernia EJ (2006) Plastic deformation and fracture of ultrafine-grained Al-Mg alloys with a bimodal grain size distribution. Acta Mater 54:1759–1766. https://doi.org/10.1016/j.actamat.2005.11.044
41. Zhou F, Nutt SR, Bampton CC, Lavernia EJ (2003) Nanostructure in an Al-Mg-Sc alloy processed by low-energy ball milling at cryogenic temperature. Metall Mater Trans A 34:1985–1992. https://doi.org/10.1007/s11661-003-0163-4
42. Chen H, Tao K, Yang B, Zhang J (2009) Nanostructured Al-Zn-Mg-Cu alloy synthesized by cryomilling and spark plasma sintering. Trans Nonferrous Met Soc China 19:1110–1115. https://doi.org/10.1016/S1003-6326(08)60415-X
43. Sadeghi B, Cavaliere P, Sadeghian B (2023) Enhancing strength and toughness of aluminum laminated composites through hybrid reinforcement using dispersion engineering. J Compos Sci 7:332. https://doi.org/10.3390/jcs7080332
44. Hua L, Hu X, Han X (2020) Microstructure evolution of annealed 7075 aluminum alloy and its influence on room-temperature plasticity. Mater Des 196:109192. https://doi.org/10.1016/j.matdes.2020.109192
45. Goswami R, Lynch S, Holroyd NJH, Knight SP, Holtz RL (2013) Evolution of grain boundary precipitates in Al 7075 upon aging and correlation with stress corrosion cracking behavior. Metall Mater Trans A 44:1268–1278. https://doi.org/10.1007/s11661-012-1413-0
46. John D, Paul T, Mohammed SMAK, Seisdedos G, Boesl B, Agarwal A (2023) Profilometry-based indentation plastometry for evaluating bulk tensile properties of aluminum-silicon carbide composites. Adv Eng Mater 25(14):2201890. https://doi.org/10.1002/adem.202201890
47. Campbell JE, Thompson RP, Dean J, Clyne TW (2019) Comparison between stress-strain plots obtained from indentation plastometry, based on residual indent profiles, and from uniaxial testing. Acta Mater 168:87–99. https://doi.org/10.1016/j.actamat.2019.02.006
48. Lama A, Sarvesha R, Garcia D, Dolmetsch T, Wang T, Eberheim R, Ross K, Agarwal A (2023) Macroscale property assessment and indentation characteristics of thick section friction stir welded AA 5083. Mater Sci Eng A 880:145306. https://doi.org/10.1016/j.msea.2023.145306
49. Rao TB (2021) Microstructural, mechanical, and wear properties characterization and strengthening mechanisms of Al7075/SiCnp composites processed through ultrasonic cavitation assisted stir-casting. Mater Sci Eng A 805:140553. https://doi.org/10.1016/j.msea.2020.140553
50. Bolshakov A, Pharr GM (1998) Influences of pileup on the measurement of mechanical properties by load and depth sensing indentation techniques. J Mater Res 13:1049–1058. https://doi.org/10.1557/JMR.1998.0146
51. Afrin N, Chen DL, Cao X, Jahazi M (2007) Strain hardening behavior of a friction stir welded magnesium alloy. Scr Mater 57:1004–1007. https://doi.org/10.1016/j.scriptamat.2007.08.001
52. Yang H, Zhang Y, Zheng S, Zaki ZI, Huang R, Lu S, Sun P, Ibrahim MM, Hou H, Li M, Yuan X, Wang X, El-Bahy ZM (2023) Dissolution behavior of dizinc magnesium phase in Al–Zn–Mg–Cu alloy. Adv Compos Hybrid Mater 6:211. https://doi.org/10.1007/s42114-023-00785-3
53. George R, Kashyap KTT, Rahul R, Yamdagni S (2005) Strengthening in carbon nanotube/aluminium (CNT/Al) composites. Scr Mater 53:1159–1163. https://doi.org/10.1016/j.scriptamat.2005.07.022
54. Zhang Z, Chen DL (2008) Contribution of Orowan strengthening effect in particulate-reinforced metal matrix nanocomposites. Mater Sci Eng A 483–484:148–152. https://doi.org/10.1016/j.msea.2006.10.184
55. Mirza FA, Chen DL (2015) An analytical model for predicting the yield strength of particulate-reinforced metal matrix nanocomposites with consideration of porosity. Materials 8:5138–5153. https://doi.org/10.3390/ma8085138
56. Liu ZY, Xiao BL, Wang WG, Ma ZY (2013) Developing high-performance aluminum matrix composites with directionally aligned carbon nanotubes by combining friction stir processing and subsequent rolling. Carbon 62:35–42. https://doi.org/10.1016/j.carbon.2013.05.049
57. Lu T, Chen C, Li P, Zhang C, Han W, Zhou Y, Suryanarayana C, Guo Z (2021) Enhanced mechanical and electrical properties of in situ synthesized nano-tungsten dispersion-strengthened copper alloy. Mater Sci Eng A 799:140161. https://doi.org/10.1016/j.msea.2020.140161
58. Chen B, Shen J, Ye X, Jia L, Li S, Umeda J, Takahashi M, Kondoh K (2017) Length effect of carbon nanotubes on the strengthening mechanisms in metal matrix composites. Acta Mater 140:317–325. https://doi.org/10.1016/j.actamat.2017.08.048
59. Mohammed SMAK, Chen DL (2020) Carbon nanotube-reinforced aluminum matrix composites. Adv Eng Mater 22:1901176. https://doi.org/10.1002/adem.201901176
60. Kelly A, Tyson WR (1965) Tensile properties of fiber-reinforced metals: Copper/tungsten and copper/molybdenum. J Mech Phys Solids 13:329–350. https://doi.org/10.1016/0022-5096(65)90035-9
61. Chierchia R, Böttcher T, Heinke H, Einfeldt S, Figge S, Hommel D (2003) Microstructure of heteroepitaxial GaN revealed by x-ray diffraction. J Appl Phys 93:8918–8925. https://doi.org/10.1063/1.1571217
62. Dong S, Zhou J, Hui D (2015) A quantitative understanding on the mechanical behaviors of carbon nanotube reinforced nano/ultrafine-grained composites. Int J Mech Sci 101–102:29–37. https://doi.org/10.1016/j.ijmecsci.2015.07.019
63. Sadeghi B, Cavaliere P (2023) Making ultra-high strengthening and toughening efficiency in hybrid reinforcing of aluminum laminated composites via dispersion engineering. Adv Powder Technol 34:104263. https://doi.org/10.1016/j.apt.2023.104263